

We are IntechOpen, the world's leading publisher of Open Access books Built by scientists, for scientists

6,900

Open access books available

186,000

International authors and editors

200M

Downloads

Our authors are among the

154

Countries delivered to

TOP 1%

most cited scientists

12.2%

Contributors from top 500 universities



WEB OF SCIENCE™

Selection of our books indexed in the Book Citation Index
in Web of Science™ Core Collection (BKCI)

Interested in publishing with us?
Contact book.department@intechopen.com

Numbers displayed above are based on latest data collected.
For more information visit www.intechopen.com



Development of Two-Phase Flow Correlation for Fluid Mixing Phenomena in Boiling Water Reactor

Hiroyuki Yoshida and Kazuyuki Takase
*Japan Atomic Energy Agency
Japan*

1. Introduction

The two-phase fluid mixing phenomena in fuel bundles of BWR plays an important role in the thermal-hydraulic performance of the fuel rod bundle, because it has strong effects on spatial distributions of the void fraction, quality and mass flow rate within it. The subchannel analysis method has been used for the prediction of the macroscopic thermal-hydraulic characteristics, such as critical power and pressure loss, of a wide variety of fuel rod bundle designs. This method evaluates the fluid mixing effects using a unique model, known as a “cross flow model”. The first successful cross flow model for gas-liquid two-phase flow was devised by Lahey and Moody (1993). In their model, cross flow phenomena were decomposed into three components, namely flow diversions caused by transverse pressure gradients, turbulent mixing caused by stochastic pressure and flow fluctuations and a void drift that is unique to gas-liquid two-phase flow.

Recently, there were studies of cross flow model improvements. Kawahara et al. (1999) presented an improved turbulent mixing model based on RMS (Root Mean Square) values of subchannel-to-subchannel differential pressure fluctuations. One of the advantages of this model was its ability to consider channel gap geometries and scales. Sumida et al.(1995) and Takemoto et al.(1997) supposed that the turbulent mixing and void drift phenomena were only transient components of the diversion cross flow caused by differential pressure fluctuations between the subchannels, and formulated the model known as the “fluctuating pressure model”. Although both models appear promising for predicting the fluid mixing phenomena however, their applicability under actual plant operation conditions is presently unclear because it is impossible to simulate differential pressure fluctuations under steam-water high-pressure conditions without relying on experimental data. Although the cross flow model remains the most popular approach today, the mechanics of the third component, the void drift, are still unclear and there is no widely accepted understanding of it yet.

In the cross flow model and subchannel analysis, two-phase flow correlations are used to evaluate effects of flow conditions on two-phase flow characteristic easily. To create, modify or confirm these correlations, “actual scale tests” those simulate flow conditions and flow channel of actual fuel bundles are required. In actual BWR, pressure and temperature equals to about 7.2MPa and 560K respectively. Then the actual scale tests take a long time and

entail great cost, development of a method that enables the thermal-hydraulic design of BWRs without these actual size tests is desired.

It is expected that large scale numerical simulations (numerical simulations by large scale computer) would replace certain large-scale tests and thermal-hydraulic information, some of which is currently difficult or impossible to measure experimentally, would be obtained. And new design method will be developed based on these numerical simulations.

For this reason we developed an advanced thermal-hydraulic design method for BWRs using innovative two-phase flow simulation technology. For this, the following are required: (1) an advanced simulation method with high accuracy prediction, (2) verification of simulation method; and, (3) analytical method to confirm or modify the correlations by detailed numerical simulation data. In this study, we are developing the method to create or modify the two-phase flow correlations for the fluid mixing phenomena in BWR based on advanced numerical simulation technic.

2. Numerical simulation method

The fluid mixing phenomena dominates water and steam distribution in the fuel bundles and is one of the most important phenomena that affect boiling transition (BT) of BWRs. Surface tension at gas-liquid interface (interface), shapes of interfaces and pressure difference fluctuation between subchannels play important roles in these phenomena. Then an advanced simulation method developed in this study must evaluate surface tension, interface shape and pressure fluctuation accurately. To satisfy these requirements, we developed an advanced simulation code: TPFIT and an advanced interface tracking method. Detail of the TPFIT and the advanced interface tracking method are explained in this section.

2.1 Governing equation and numerical simulation

To calculate surface tension and interface shapes by realistic computational resources, the TPFIT adopt interface tracking method. In two-phase flow in rod bundles, compressibility of steam has important influence for pressure difference fluctuation between subchannels. In TPFIT, considering the time-dependent Navier-Stokes equation for two phase compressible flow, conservative equations of mass of liquid, mass of gas, momentum and energy are described as follows:

Mass of liquid:

$$\frac{\partial(\rho f)_l}{\partial t} + \frac{\partial u_k(\rho f)_l}{\partial x_k} = 0 \quad (1)$$

Mass of gas:

$$\frac{\partial(\rho f)_g}{\partial t} + \frac{\partial u_k(\rho f)_g}{\partial x_k} = 0 \quad (2)$$

Momentum:

$$\frac{\partial u_i}{\partial t} + u_k \frac{\partial u_i}{\partial x_k} = -\frac{\partial p}{\partial x_i} + \frac{1}{\rho} \frac{\partial \tau_{ik}}{\partial x_k} + g_i + \sigma_i \quad (3)$$

Energy:

$$\frac{\partial e}{\partial t} + u_k \frac{\partial e}{\partial x_k} = -\frac{p}{\rho} \frac{\partial u_k}{\partial x_k} + \frac{1}{\rho} \frac{\partial}{\partial x_k} \left(\lambda \frac{\partial T}{\partial x_k} \right) + q \quad (4)$$

where u , p , e , T are velocity, static pressure, internal energy and temperature, and g and σ in the momentum equation are gravity and surface tension force, respectively. In above equations, subscripts g and l are used to represent gas and liquid phases. The mass of liquid and gas phases in two phase flow are defined as following equation.

$$\begin{aligned} (\rho f)_l &= \rho_l f_l \\ (\rho f)_g &= \rho_g f_g \end{aligned} \quad (5)$$

In Eq. (5), f is volume fraction of fluid, and Volume fraction of gas phase is evaluated by use of volume fraction of liquid.

$$f_g = 1 - f_l \quad (6)$$

Two-phase fluid density ρ is calculated as sum of mass of both phases:

$$\rho = (\rho f)_l + (\rho f)_g \quad (7)$$

Eqs. (1) and (2) are solved in the advanced interface tracking method described in sec.2.2. The momentum equation (Eq. (3)) is solved by the CIP (Cubic Interpolated Pseudo-particle) method (Yabe and Aoki, 1991). The energy equation (Eq. (4)) is used to obtain the Poisson equation for static pressure. Temperature is estimated by means of a fluid property routine based on the static pressure and local density of both phases. The ILUCGS method is used to solve the Poisson equation for static pressure. In the TPFIT code, a Cartesian coordinate system and staggered grid are used. The surface tension force in the momentum equation is estimated using the CSF model (Blackbill et al., 1992). In the CSF model, volume fraction of liquid f_l is required and evaluated in the advanced interface tracking method, too. The local viscosities and thermal conductivities of liquid and gas were evaluated using solved static pressure and temperature fields based on the fluid property routine.

2.2 Outline of advanced interface tracking method

The fundamental concept of the advanced interface tracking method is quite simple. That is, a transported volume of liquid and gas between neighboring calculation control volumes during each time step is calculated through the movement of approximated gas-liquid interfaces, as estimated in the Lagrangian system. Schematic drawings of the major three operational steps within each time step in the two-dimensional case are shown in Figure 1.

In the first step (reconstruction step), as shown in Figure 1 (a), a gas-liquid interface in each control area for calculations is reconstructed, taking account of the liquid fraction represented by it and its surroundings. In the reconstruction step, the gas-liquid interface is approximated by a linear function: $F(\mathbf{x})$ as same as PLIC (Gueyffier, et al., 1999) method (see Fig.2 for 3-dimensional case). The function $F(\mathbf{x})$ is expressed as follows:

$$F(\mathbf{x}) = \sum_{i=1}^{n_m} a_i x_i + b, \quad \mathbf{x} = (x_1, x_2, x_3) \quad (8)$$

In the equation, n_m represents dimension of simulation, and is 2 or 3. x_i is the coordinate position of the definition point of scalar quantities. A unit normal vector to the interface $\mathbf{a} = (a_1, a_2, a_3)$ and segment b in Eq.(8) must be estimated.

To evaluate the function $f(\mathbf{x})$, we assumed that the interface exists in the position where volume fraction of liquid f_l equals to 0.5. By least-squares method (choose eight nearest neighbors for 2-dimensional case, 26 nearest neighbors for 3-dimensional case), linear function is obtained.

$$F(\mathbf{x}) = f_l - 0.5 = \sum_{i=1}^{n_m} a_i x_i + b_0 \quad (9)$$

In the equation, b_0 is segment of linear function evaluated by least square method. Control volume is divided into two polyhedrons by the linear functions. If gray polyhedron in Fig.2 corresponds to liquid region in control volume, volume of this polyhedron: V_l must be equals to proper volume of liquid. Thus,

$$V_l = f_l \Delta V \quad (10)$$

where ΔV is a volume of computational cell given by following equation for 3-dimensional cases.

$$\Delta V = \Delta x_1 \cdot \Delta x_2 \cdot \Delta x_3 \quad (11)$$

To satisfy Eq. (10), the segment b is adjusted as fraction $V_l/\Delta V$ agrees with volumetric fraction of fluid. Between the volume of fluid V_l and segment b , there is the relation that is expressed as the following equation for three dimensional cases.

$$V_m = \frac{1}{6a_1 a_2 a_3} \left\{ b^3 - \sum_{i=1}^3 [\max(b - a_i \Delta x_i, 0)]^3 - \sum_{i=1}^3 [\max(b - b_m + a_i \Delta x_i, 0)]^3 \right\} \quad (12)$$

In this equation, b_m is the maximum value that b can take:

$$b_m = \sum_{i=1}^3 a_i \Delta x_i \quad (13)$$

In this study, the Newton's method is used to estimate the segment b that satisfies Eq. (12). In the next step (transportation step), polyhedrons within each control volume are transported along a surrounding velocity field (Fig.1 (b)). Some parts of the volume of this polyhedron are transported to surrounding control volume. For example, in Fig.1(b), δV is transferred from control volume 1 to control volume 2. Each transferred volume of liquid is calculated in this step. And each transferred volume of gas is also calculated by a procedure same as the volume of liquid.

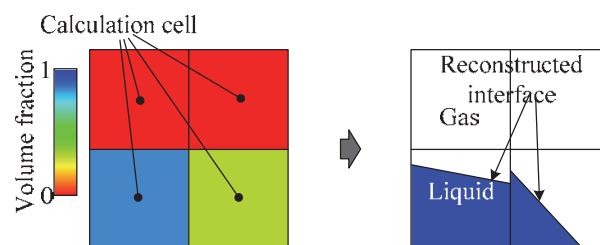


Fig. 1. (a) Reconstruction step

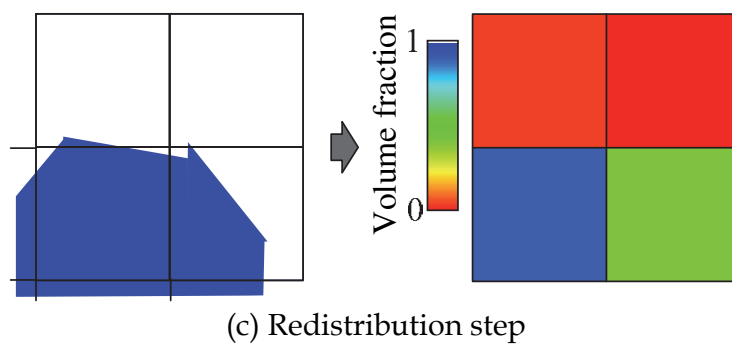
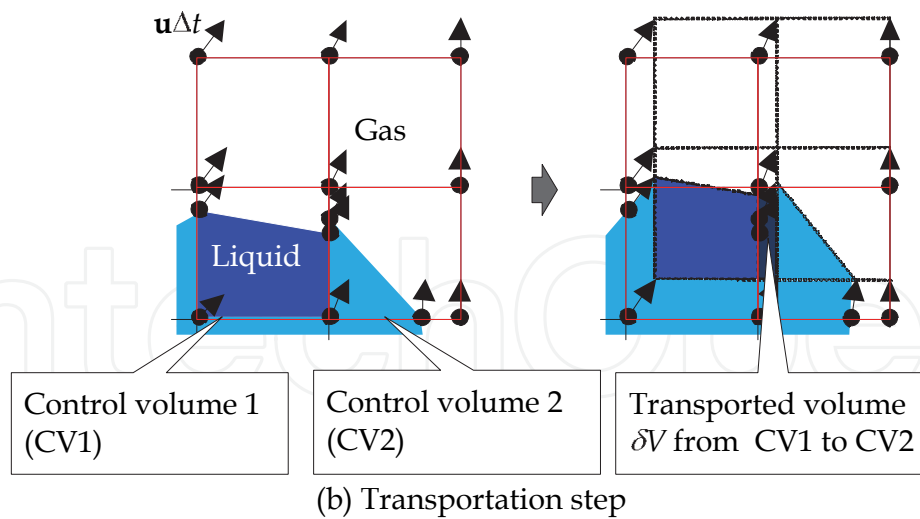


Fig. 1. Schematic drawings of volume fraction transport calculation using the advanced interface tracking method (2-dimensional case).

In transportation step, transfer volume of both phases is calculated. In the last step (redistribution step), as shown in Fig.1(c), transferred mass of both phases can be evaluated by multiplying density by transferred volume. Mass at new time step can be calculated by summing these transferred mass.

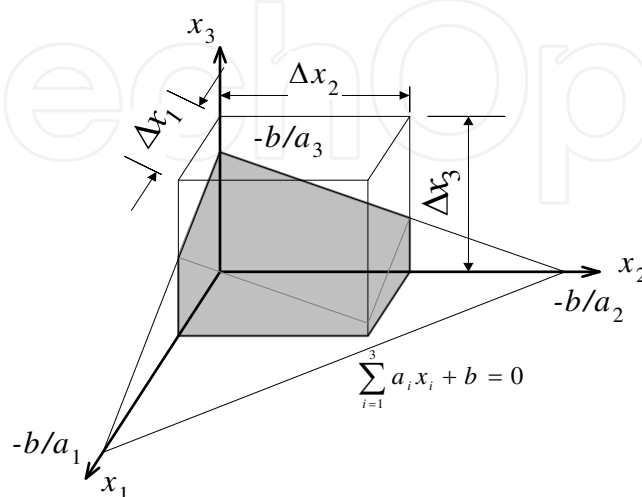


Fig. 2. Approximated fluid segment in control volume (3-dimensional case).

3. Validation of TPFIT for fluid mixing phenomena

We try to validate the TPFIT with the advanced interface tracking method developed in this study for fluid mixing phenomena.

3.1 Verification and validation of TPFIT for simple flow configuration

Before validate the TPFIT for fluid mixing phenomena, we check basic performance of the TPFIT for two-phase flow by performing numerical simulation in simple flow configuration

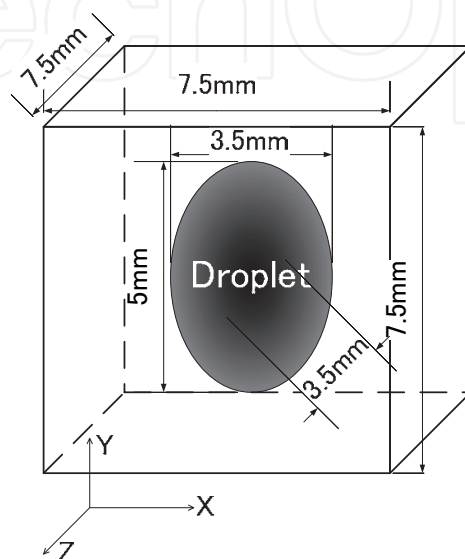


Fig. 3. Initial arrangement of droplet.

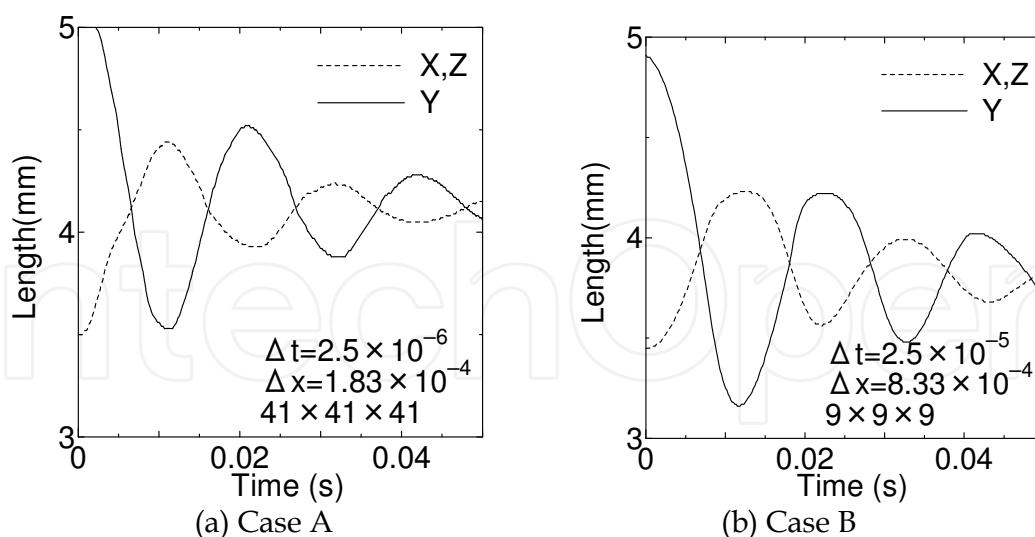


Fig. 4. Time change of diameters of droplet.

3.1.1 Vibrating droplet under the zero gravity

In order to verify the potential of the advanced interface tracking method, 3-dimensional analyses of the vibration of a liquid drop under zero gravity were carried out. Initial arrangement of the droplet is shown in Fig.3. In the simulations, two computational grids

were used, one is a fine grid (41×41×41, case A) and another is a course grid (9×9×9, case B). Time changes of diameters of the droplet are shown in Fig.4. The vibration cycle is about 0.022 seconds and agrees with the theoretical value that expressed as following equation (Rayleigh, 1879).

$$\tau = \pi \sqrt{\frac{\rho_l r^3}{2\sigma}} \tag{14}$$

The results of the case A and those of the case B are almost the same, and the effect of the different grid number is small. The diffusion at the gas-liquid interface was not observed. Then we confirmed the effectiveness of the advanced interface tracking method.

3.1.2 Liquid film falling down on inclined flat plate

In the fluid mixing phenomena, bubble, bubble/slug, slug and slug/churn flow are important. However, in slug flow, liquid film is observed between slug bubble and wall. Then verification of the TPFIT must be performed for film flow.

The TPFIT code was applied to numerical simulation of liquid film falling down on inclined flat plate. Simulations were performed with the same conditions as the experiment by Moran et al. (2003) (see Fig.5). Physical properties of the liquid were as follows: kinematic viscosity, $\nu_l=2\times 10^{-5}$ m²/s, density, $\rho_l=960$ kg/m³, and surface tension, $\sigma=2.06\times 10^{-2}$ N/m. And air properties at 300K and atmospheric pressure were used as gas properties. On all walls, non-slip boundary condition was assigned, and inlet pressure was fixed at atmospheric pressure.

The flow conditions were summarized in Table 1. The analysis conditions were set up to compare the probability density function (PDF) of local film thickness with the experimental results. In the table 1, δ_N represents Nusselt's mean film thickness (Nusselt, 1916), and is evaluated by the following equation:

$$\delta_N = \left(\frac{3\nu_l J}{g_z} \right)^{1/3} \tag{15}$$

In this equation, g_z is flow direction acceleration by gravity force, and J is mass flow rate of the liquid.

Case	Inlet flow rate J (l/min)	Film Reynolds number	δ_{ave_exp}	δ_{ave_cal}	δ_N
1	0.333	13	0.91	0.85	0.84
2	2.55	106	1.73	1.67	1.66
3	5.45	220	2.31	2.15	2.14

Table 1. Numerical conditions.

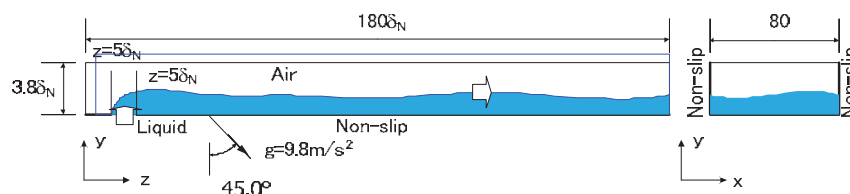


Fig. 5. Analytical geometry of a liquid film.

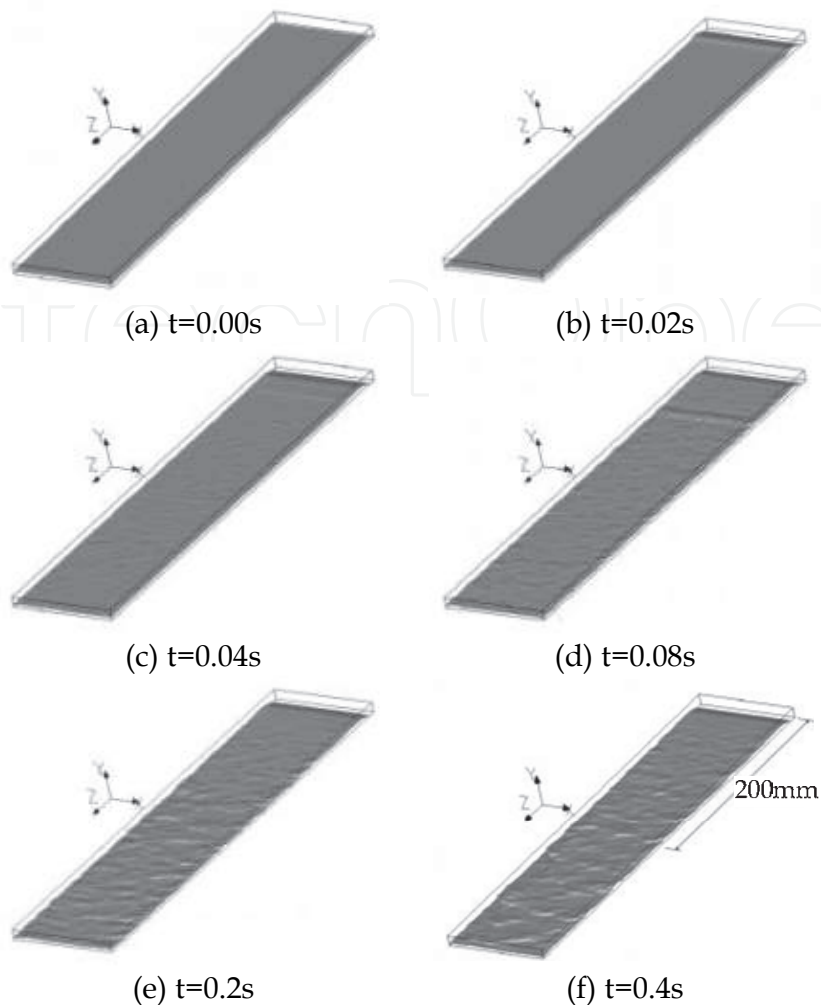


Fig. 6. Observed liquid film shapes.

Figure 6 shows snapshot of the numerical results of the Case 3. In this study, the calculated gas-liquid interfaces were defined as isosurface at a volume fraction of liquid of 0.5. In 0.02s, two-dimensional wave was observed near liquid inlet section, and this wave moves to the downstream section. From 0.04 seconds later, small three-dimensional waves occurred on the surface of the liquid film. After that, these small waves gradually becomes big until $t=0.2s$. At $t=0.4s$, the liquid film exhibited a smooth, flat gas-liquid interface upon immediate entrance to the test section, but after a short distance small, small ripples were observed at the interface. At approximately 200mm (about $z=100 \delta_N$) from the inlet, the small ripples developed into a three-dimensional structure characterized by large waves, and wave structures were almost developed at this point. In general, the degree of waviness increased with increasing film Reynolds number. The average local film thicknesses in the numerical result (δ_{ave_cal}) at $x=20mm$ and $z=175 \delta_N$ are shown in Table 1 and almost agreed with Nusselt's mean film thickness. However, δ_{ave_cal} were slightly smaller than the average film thickness in the experimental results (δ_{ave_exp}).

The probability density functions (PDF) of liquid film thickness at $x=20mm$ and $z=175 \delta_N$ were evaluated to compare numerical results with the experimental results quantitatively. Figure 7 shows the PDF of film thickness. At low Reynolds numbers ($Re_f=13$), the PDF distributions showed a sharp peak (first peak) at about average film thickness, but remained

close to zero for greater thickness values, indicating existence of few waves. At low film Reynolds number, the position and height of the first peak agreed well in the analysis and experiment.

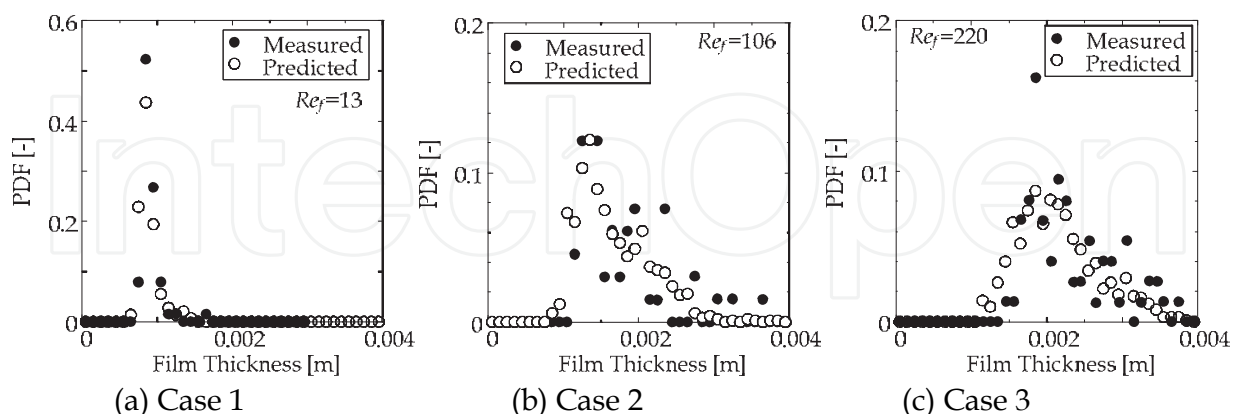


Fig. 7. Probability density function of liquid film thickness.

In the experimental results, at relatively high Reynolds number ($Re_f=106$ and 220), additional smaller peaks (second peaks) appeared to the right of the main peaks. Because the sampling numbers (n_s) used in the processing of the experimental data ($n_s = 60$) were smaller than those in the numerical results ($n_s = 1200$), scattered results were observed in the experimental PDF distributions. As shown in Fig.8, the numerical result agreed well with the experimental result including existence of second peaks and these positions. The predicted values of minimum liquid film thickness by the numerical simulations were slightly smaller than those measured by the experiments without relying on the mass flow rate of the liquid. It is thought that because the predicted minimum liquid film thicknesses were thin, the average liquid film thicknesses became smaller in comparison with the experimental results.

3.1.3 Bubbly and slug flow in square duct

By two-phase correlations for fluid mixing phenomena, volume or mass cross flow rate or mixing coefficients are evaluated. Then volume and mass conservation of two-phase flow is important function. As mentioned above, volume conservation equations for both phases are not solved, and the TPFIT has no special treatment to keep volume conservation. Then we must check volume conservation of the TPFIT. In two-phase flow fluid mixing phenomena, the maximum value of mixing gas flow rate is around 10% of gas flow rate in flow channel. An error of the volume conservation must be done below 1% if we want to predict mixing coefficient with accuracy of less than 10%.

Case	Fluid	Inlet	Inlet void fraction: α_{in}	Inlet velocity: w_{in}
1	Air-water at 0.1MPa and 300K	A	0.307	0.5 m/s
2		B	0.111	
3	Steam-water at 7.2MPa and 560K	A	0.307	
4		B	0.111	

Table 2. Numerical condition for bubbly flow in square duct.

To check volume conservation, the TPFIT was applied to bubbly and slug flow in square duct. Numerical domain is shown in Fig.8 (a), and numerical conditions are shown in table 2. In the simulations, air-water and steam-water two-phase flow were used. Air-water two-phase flow at atmospheric pressure is used as working fluid in many experimental researches, and the TPFIT was applied to these experiments for validation. Then we used in this simulation. Steam-water two-phase flow at 7.2MPa and 560K (saturation temperature at 7.2MPa) is appeared in real (actual) reactor conditions. Two-phase flow correlations will be checked or examined at this conditions, we also used in this simulation. On all walls, non-slip boundary condition was assigned, and inlet velocity and volume fraction of liquid were fixed. Outlet pressure was also fixed at atmospheric pressure or 7.2MPa.

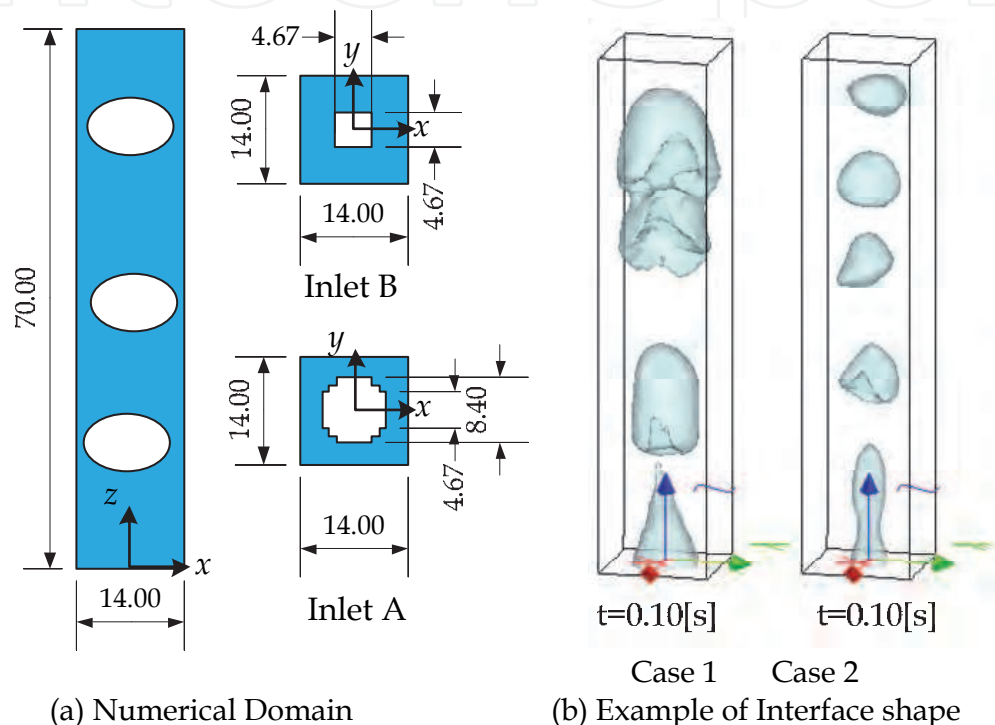


Fig. 8. Numerical domain and example of interface shape.

Figure.8 (b) shows example of interface shapes. Different two-phase flows were formed in a square duct by the difference in inlet volume fraction. And complicated interface shapes were observed in higher volume fraction case (Case 1). Figure 9 shows evaluated volume conservation error. In this figure, E_{vol} was volume conservation error and defined as following equation.

$$E_{vol} = \frac{Vol_g}{Vol_{g,in}} - 1, \quad (16)$$

where Vol_g is calculated total gas volume in a square duct by use of simulated results. And $Vol_{g,in}$ is total gas volume calculated by use of inlet condition of simulations:

$$Vol_{g,in} = \alpha_{in} \cdot w_{in} \cdot A \cdot t, \quad (17)$$

where, A is area of square duct ($=14 \times 14 = 196 \text{mm}^2$), t is time. In Case 1 and 2, differences between gas density and liquid density was relatively large, and effects of compressibility of

gas was also large. Then, large fluctuation of E_{vol} in Case 1 and 2 was observed. However, except these fluctuations, the maximum value of volume conservation error: E_{vol} were less than 0.2%. Therefore, it was confirmed that the TPFIT has enough performance of volume conservation to simulate two-phase flow fluid mixing phenomena.

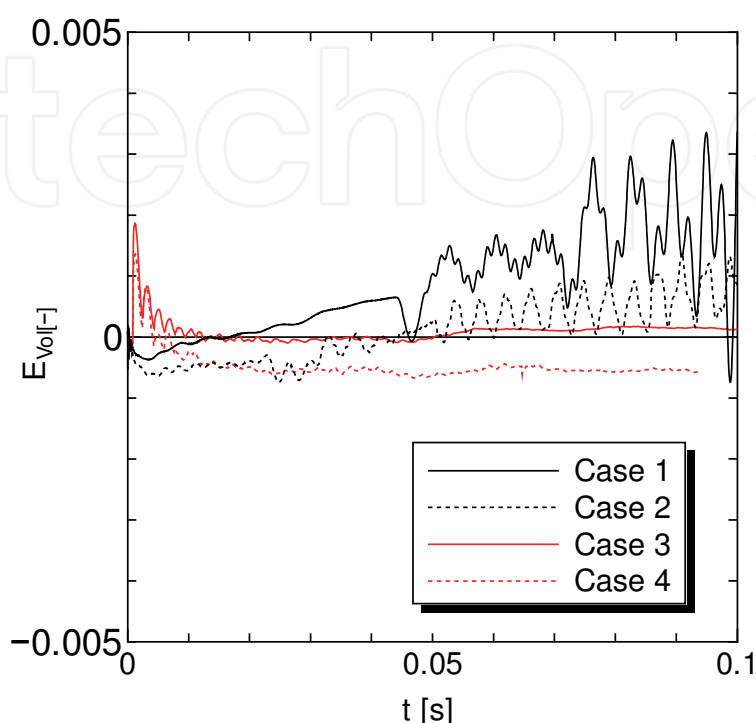


Fig. 9. Evaluated volume conservation error for two-phase flow in square duct.

3.2 Verification for fluid mixing phenomena by experimental data

In the next step, we must validate TPFIT for fluid mixing phenomena. To evaluate TPFIT performance for two-phase flow fluid mixing phenomena between the subchannels, numerical simulations for two-phase flow fluid mixing tests were performed.

3.2.1 Air-water fluid mixing test

TPFIT code was applied to 2-channel air-water mixing tests (Yoshida, 2007). The dimension of calculated test channel is shown in Fig.10 (a). The test channel, which consists of two parallel subchannels with an 8×8 mm square cross section and the interconnection, is 220 mm long and air and water flow upwards in it. The interconnection's gap clearance, horizontal and vertical length are 1.0 mm, 5.0 mm and 20 mm respectively. An irregular mesh division in the Cartesian system was adopted and two subchannels and the interconnection were formed by using obstacles as shown in Fig.11. The total number of effective control volumes was 428,680 respectively. The fluid mixing was observed at interconnection in the experiments. A non-slip wall, constant exit pressure and constant inlet velocity were selected as boundary conditions for each subchannel. The time step was controlled with a typical safety factor of 0.2 to keep it lower than the limitation value given by the Courant condition and stability condition of the CSF model. Calculation conditions are shown in Table 3.

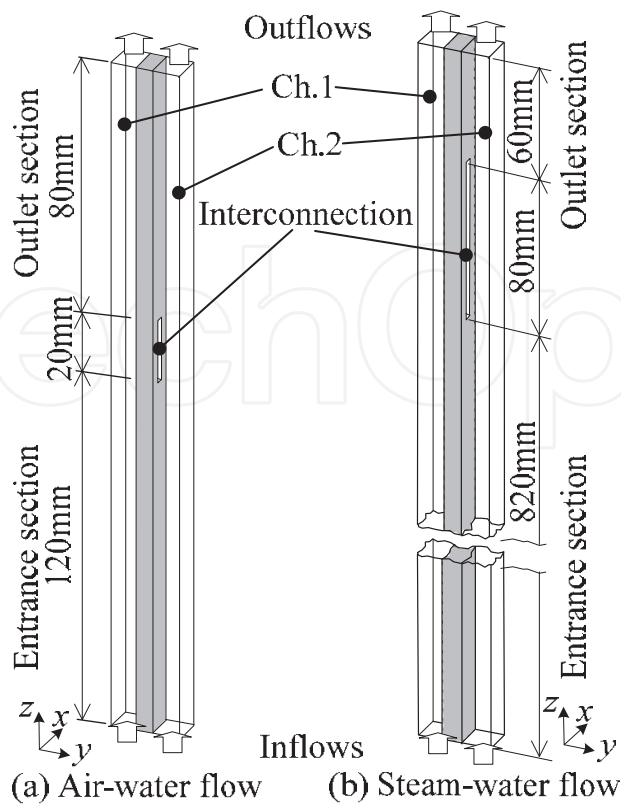


Fig. 10. Calculated test channel.

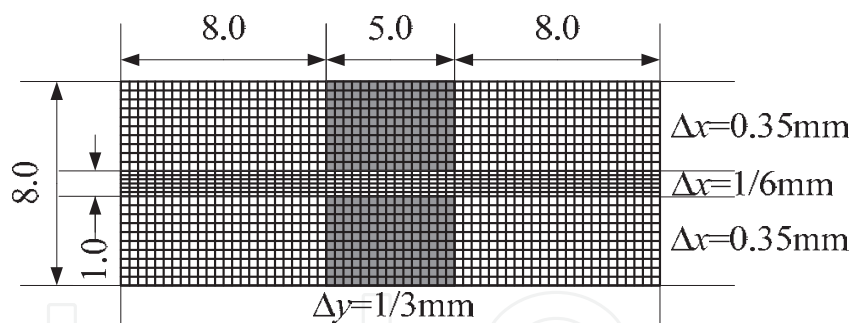


Fig. 11. Calculation meshes in channel cross section for air-water fluid mixing test.

Water inlet velocity (m/s)		Injected air volume (cc)	
Ch.1	Ch.2	Ch.1	Ch.2
0.26	0.26	1.27	1.50

Table 3. Air-water flow calculation condition.

The slug behavior observed around the interconnection is shown in Fig.12 (a). Once the top of an ascending air slug in Ch.1 reaches the center height of the interconnection, part of it starts to be drawn toward Ch. 2. Then the tip of stretched part of the air slug flows into Ch.2 through the interconnection and is separated to form a single bubble. The calculated air slug behavior is shown in Fig.12 (b). As shown in Fig.12 (b), any intrusion of air into the interconnection as well as any separation of the air slug can be effectively calculated. The

moved bubble volumes from Ch.1 to Ch.2 were estimated to be 0.087cc in the observation and 0.094cc in the calculation.

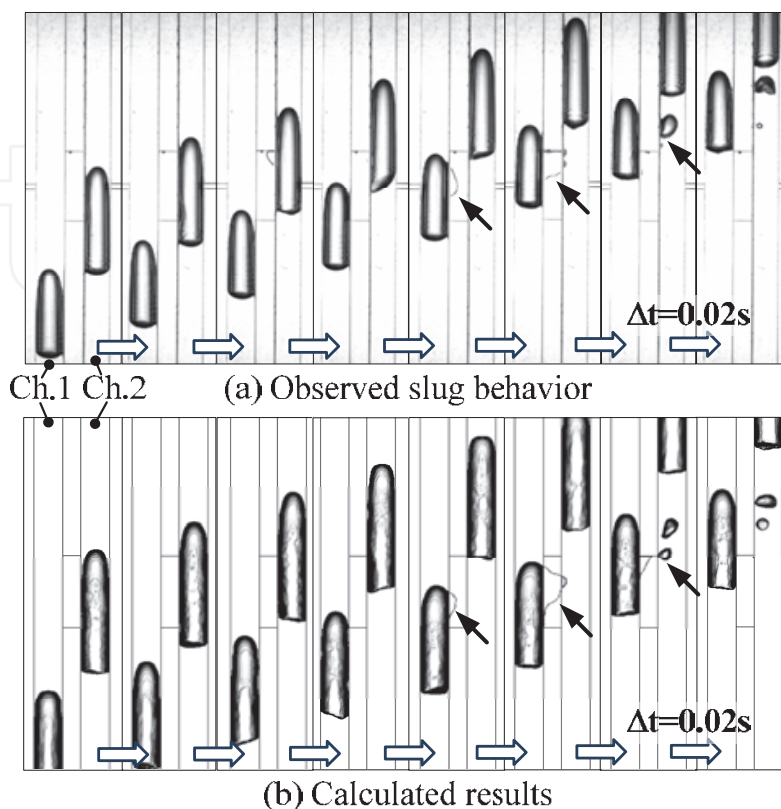


Fig. 12. Observed and calculated slug behavior of air-water fluid mixing test around the interconnection.

3.2.2 Steam-water fluid mixing under high pressure

The TPFIT was applied to steam water fluid mixing test (Yoshida, 2007). Calculated test channels used in these simulations are shown in Fig.10 (b). The calculation conditions are shown in Table 4. An irregular mesh division in the Cartesian system was adopted and two subchannels and the interconnection were formed by using obstacles as shown in Fig.13. The total number of effective control volumes was 2,647,400 respectively. A non-slip wall, constant exit pressure, and constant inlet velocity were selected as boundary conditions for each subchannel.

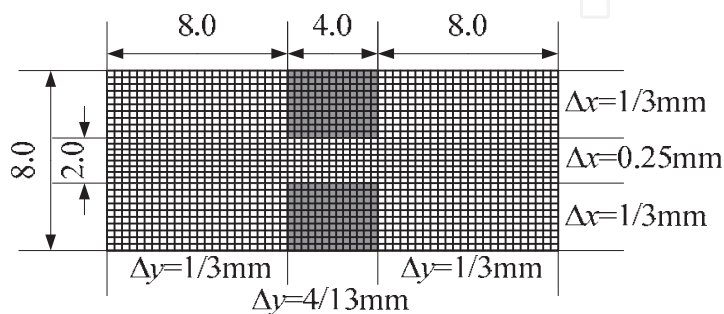


Fig. 13. Calculation meshes in channel cross section for steam-water fluid mixing test.

Inlet mass flow rate (kg/s)		Inlet quality (%)	
Ch.1	Ch.2	Ch.1	Ch.2
0.44	0.23	0.0	0.47

Table 4. Steam-water flow calculation condition.

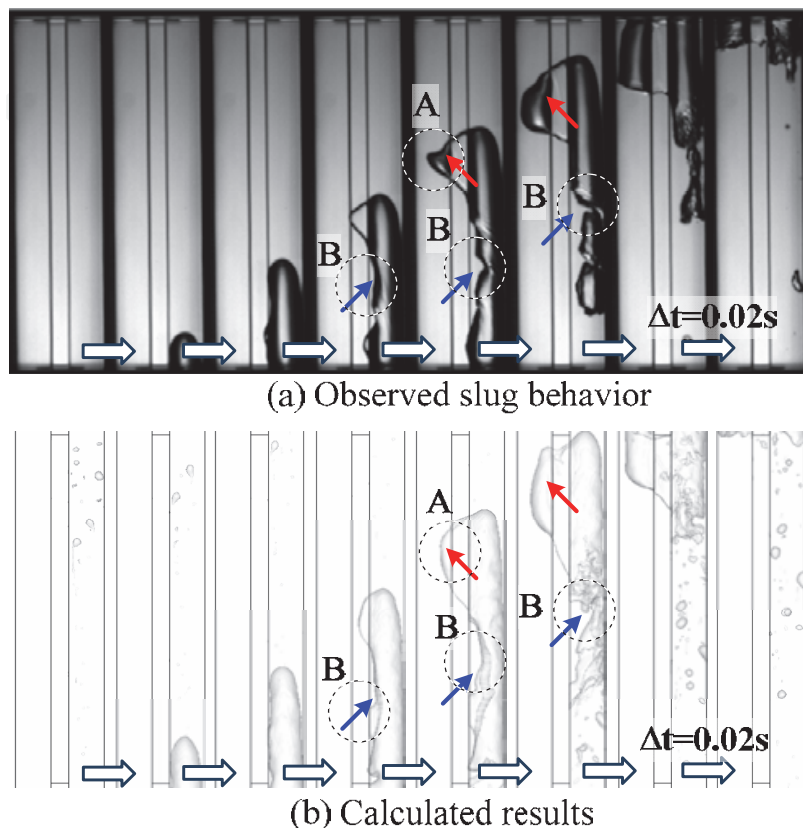


Fig. 14. Observed and calculated slug behavior of steam-water fluid mixing test around the interconnection.

The slug behaviors observed and calculated around the interconnection is shown in Fig.14. As shown in Fig.14 (a), a part of single steam slug in Ch.2 intrudes to the Ch.1 through the interconnection. Averaged slug length is about 56 mm, and observed major slug characteristic behavior is as follows.

- Steam intrusion from Ch.2 to Ch.1 is firstly occurred at the upper part of the steam slug ("A" in the Fig.14).
- Constriction is generated at the center part of the steam slug by water flow from Ch1 to Ch.2, and the steam slug break up ("B" in the Fig.14).

As shown in Fig.14 (b), the occurrence of intrusion of steam from the Ch.2 to the Ch.1 can be effectively calculated, and the calculated amount of steam penetration into the interconnection looks quite similar to the observed one. Predicted slug length is about 59 mm, and almost same as the observed one. As shown in Fig.14 (b), the major slug characteristic behavior observed in the experiment was reproduced in the numerical simulation by TPFIT code.

The measured and calculated differential pressure and cross flow rate between Ch.1 and Ch.2 for steam-water flow are shown in Figs.15 and 16 respectively. The calculated values of the differential pressure and the cross flow rate agreed well with the measured values.

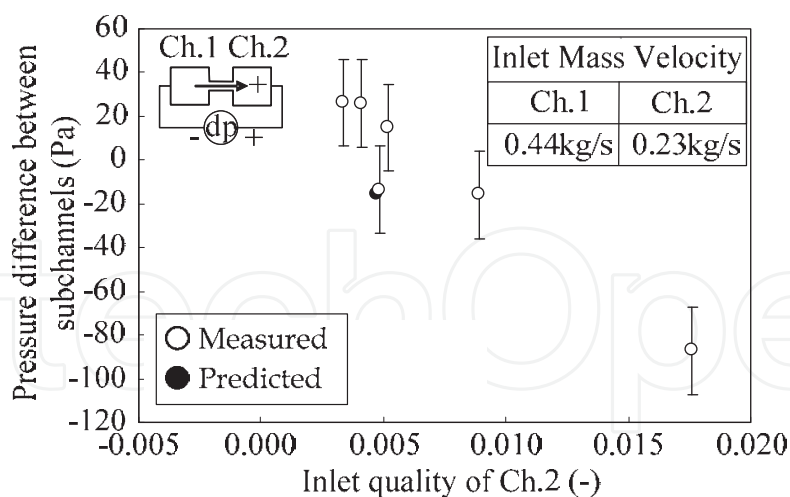


Fig. 15. Measured and calculated pressure difference between subchannels.

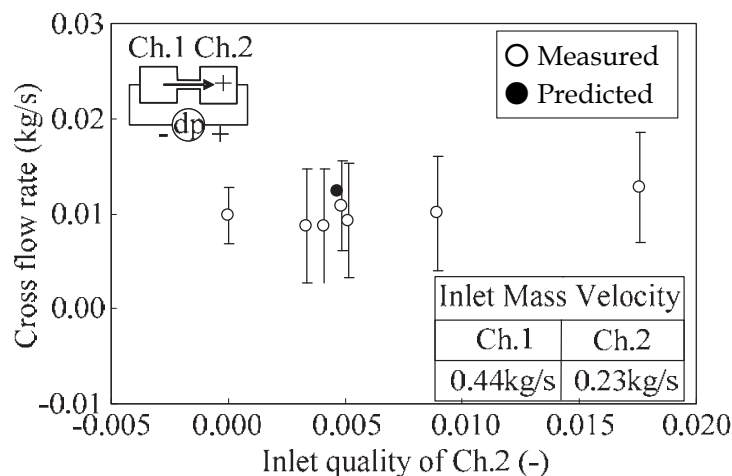


Fig. 16. Measured and calculated pressure difference between subchannels.

3.2.3 Numerical simulation of air-water two-phase flow in modeled 2 subchannels

The TPFIT code was applied to experimental analyses of the existing 2-channel fluid mixing experiments (Sumida, 1995), and comparisons between measured and calculated results were carried. In the experiments, the differential pressure between the subchannel at the center height of the mixing section and the exit air and water flow rate of each subchannel were measured.

Numerical analyses of air-water flow fluid mixing were applied between the length of -100mm and +60mm from the lower edge of the mixing section in the flow direction of the test channel as shown in Fig.17 (a). The flow area is divided into two channels by a flat plate (partition plate). At the upper part of the partition plate, there was a narrow slit, through which the channels were connected. The flow channel was divided into 3 parts, developing section, mixing section and outlet section. The narrow slit was located in the mixing section, and fluid mixing was occurred at this section. The developing section was set up to get developed flow at inlet of the mixing section. The outlet section was located at top of the calculated test channel to let out air-water two-phase flow smoothly.

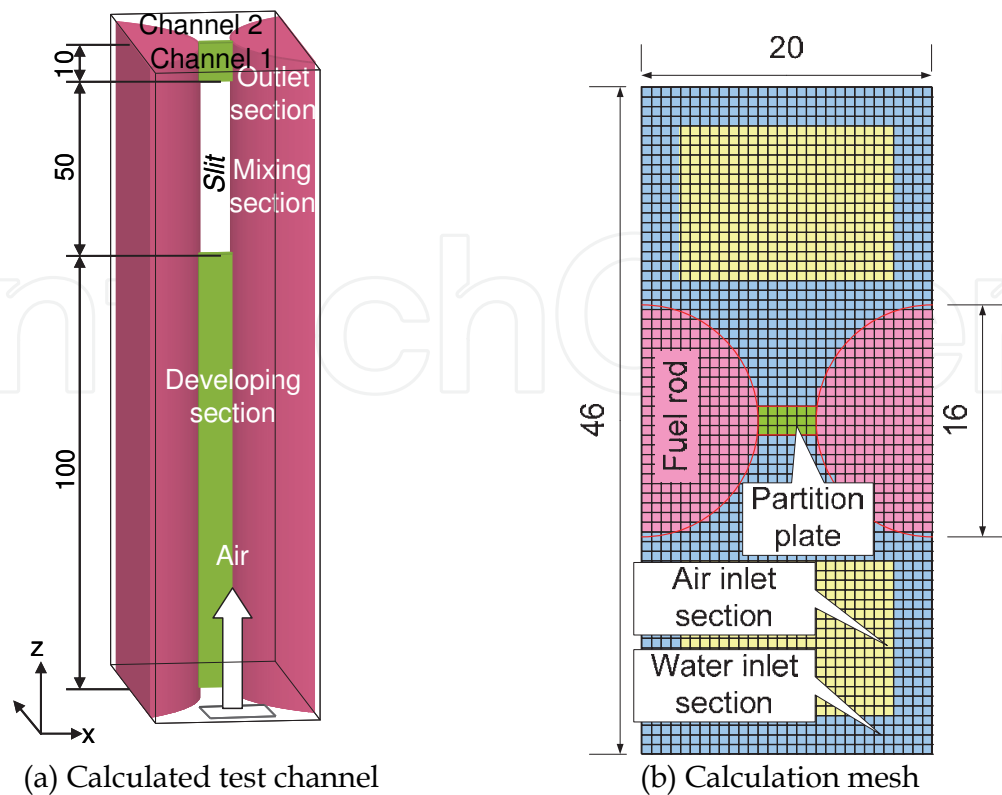


Fig. 17. Dimensions of calculated test channel and calculation meshes in channel cross section for air-water two-phase flow.

Regular mesh division in the Cartesian system was adopted and two subchannels and the interconnection were formed by using obstacles as shown in Fig.17 (b). The calculation mesh size was set to $2/3$ mm to satisfy the condition that the number of the calculation meshes of gap region must be more than 6, and the total number of the calculation meshes was 496,800. A non-slip wall, constant exit pressure and constant inlet velocity were selected as boundary conditions for each subchannel. The effects of the contact angle of the water on the channel walls were set to 15 degree.

Case	Inlet liquid mass flux ($\text{kg}/\text{m}^2\text{s}$)		Inlet quality (%)	
	Ch.1	Ch.2	Ch.1	Ch.2
L1	370		0.0013	0.0007
L2				0.0013
L3				0.0019
L4				0.0026
H1	277		0.0022	0.0011
H2				0.0022
H3				0.0033
H4				0.0044

Table 5. Air-water flow calculation condition.

Air and water were injected through the air and water inlet section located at lower part of the modeled test channel (see Fig.17 (a)). The area of the air and water inlet section was

constant, and the inlet air and water velocities were varied to simulate experimental conditions. Eight cases of air-water two-phase flow simulations were performed and calculation conditions were summarized in Table 5. In the simulation, inlet liquid mass flux for 2 subchannels was same. Outlet pressure and inlet temperature of air and water is set to atmospheric pressure and room temperature respectively. In the case H1 to H4, inlet liquid mass flux was set to 370 (kg/s), and inlet quality was relatively low. In the case H1 to 4, inlet liquid mass flux was set to 277 (kg/s), and inlet quality was relatively high. Then, we describe case L1 to L4 with “low quality cases”, and case H1 to H4 with “high quality cases”.

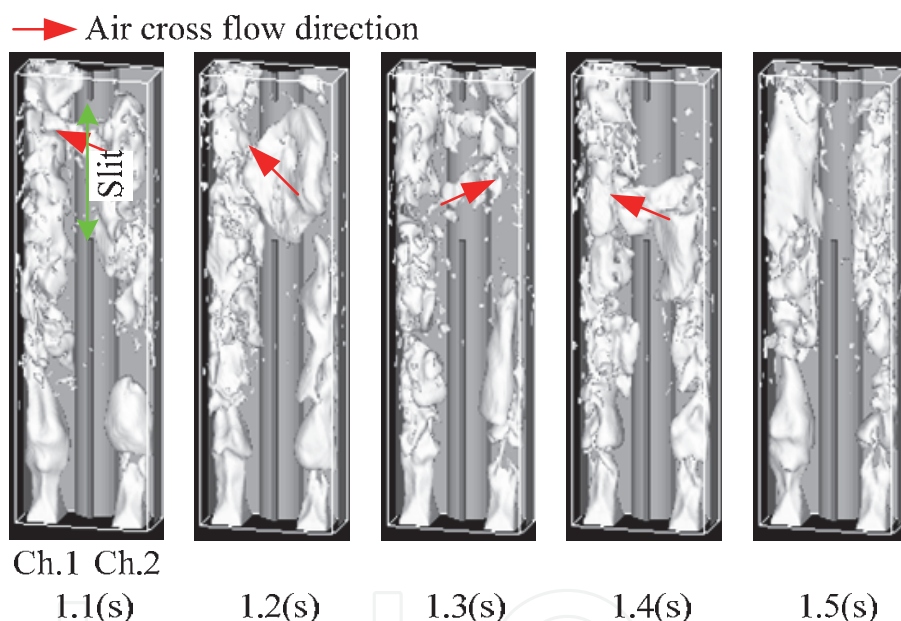


Fig. 18. Observed and calculated slug behavior of case H1.

Example of the calculated slug behaviors in the test channel are shown in Fig.18. As shown in Fig.18, the fluid mixing was observed at the gap between the subchannels. The measured and calculated differential pressure between the 2 subchannels is shown in Fig.19. The pressure differences at the longitudinal center of the mixing section were measured and calculated. In the figure, time averaged values (“Average”) and standard deviation of fluctuating values (“Fluctuation” in the figure) of differential pressure are shown. The degree of fluctuation of values was evaluated by the following equation:

$$\sigma_{\Delta p} = \sqrt{(\Delta p_T - \Delta p_s)^2} \tag{18}$$

where,

$$\Delta p_s = \overline{\Delta p_T} \tag{19}$$

Δp_i : instantaneous value of differential pressure.

Δp_s : time averaged value of differential pressure

Underestimations tended to be made in cases of low inlet quality, but the numerical results agreed well with the experimental results, both qualitatively and quantitatively.

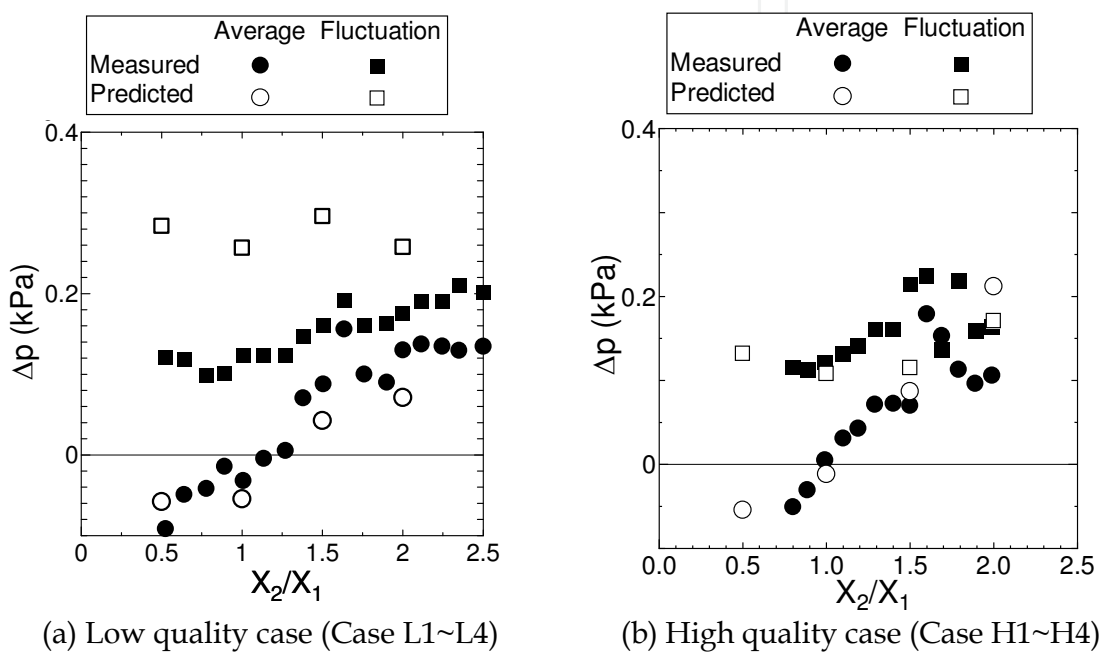


Fig. 19. Measured and calculated pressure difference between subchannels.

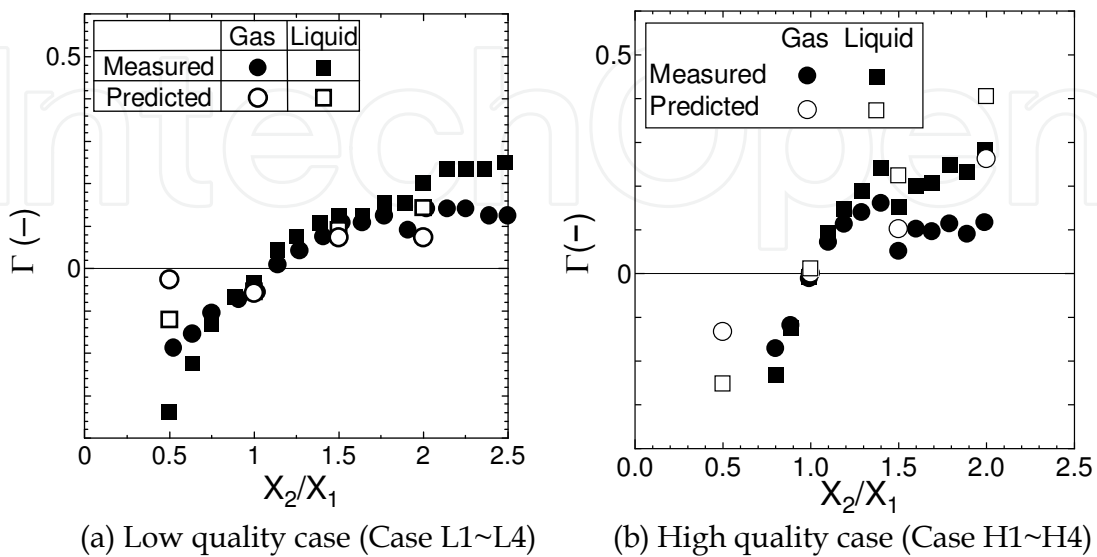


Fig. 20. Measured and calculated mixing coefficient.

The measured and calculated mixing coefficients of both phases for air-water cases are shown in Fig.20. The mixing coefficients of gas and liquid are defined as below (Sumida, 1995):

$$\Gamma_m = \frac{w_m}{W_{m1} + W_{m2}} \quad (20)$$

where,

W_{m1} : Inlet mass flow rate of m phase for channel 1

W_{m2} : Inlet mass flow rate of m phase for channel 2

w_m : Moved mass flow rate from channel 1 to channel 2

Underestimations tended to be made in cases of low inlet quality, but the numerical results agreed well the experimental results. These underestimations of mixing coefficients corresponded to those of differential pressure. It seems that a main cause of underestimations was overestimation of the flow resistance in the gap region due to insufficient spatial resolution when gas velocity is relatively low.

4. Development of two-phase flow correlation for fluid mixing phenomena

4.1 Evaluation of existing correlations for fluid mixing phenomena

Innovative water reactor for flexible fuel cycle (FLWR) is one of new generation light water reactor and has been developed at Japan Atomic Energy Agency (Uchikawa, 2007). In order to achieve a conversion ratio higher than unity, a hexagonal tight-lattice rod bundle with about 1mm of gap width was adopted. Due to narrower rod gaps and the channels being surrounded by rods, bubble/slug-to-bubble/slug and bubble/slug-to-wall interactions may occur more frequently within the FLWRs core than in those of current BWRs, and these may affect the two-fluid mixing characteristics by way of the deformation, separation and coalescence of bubbles/slugs caused by the interactions.

4.1.1 Analytical conditions

In this section, to evaluate the existing two-phase flow correlation for fluid mixing phenomena, two-phase flow in 2 modeled subchannels for BWRs and FLWRs fuel bundles were performed ("BWR cases" and "FLWR cases"). For this, 16 cases of two-phase flow simulations were performed (see table 6 and 7).

Case	Inlet liquid mass flux (kg/m ² s)		Inlet quality (%)	
	Ch.1	Ch.2	Ch.1	Ch.2
B1	1400		0.0067	0.0264
B2			0.0134	
B3			0.0264	
B4			0.0513	
B5			0.0184	0.0362
B6			0.0362	
B7			0.0533	
B8			0.0699	

Table 6. Calculation conditions for fluid mixing phenomena in BWRs fuel bundle.

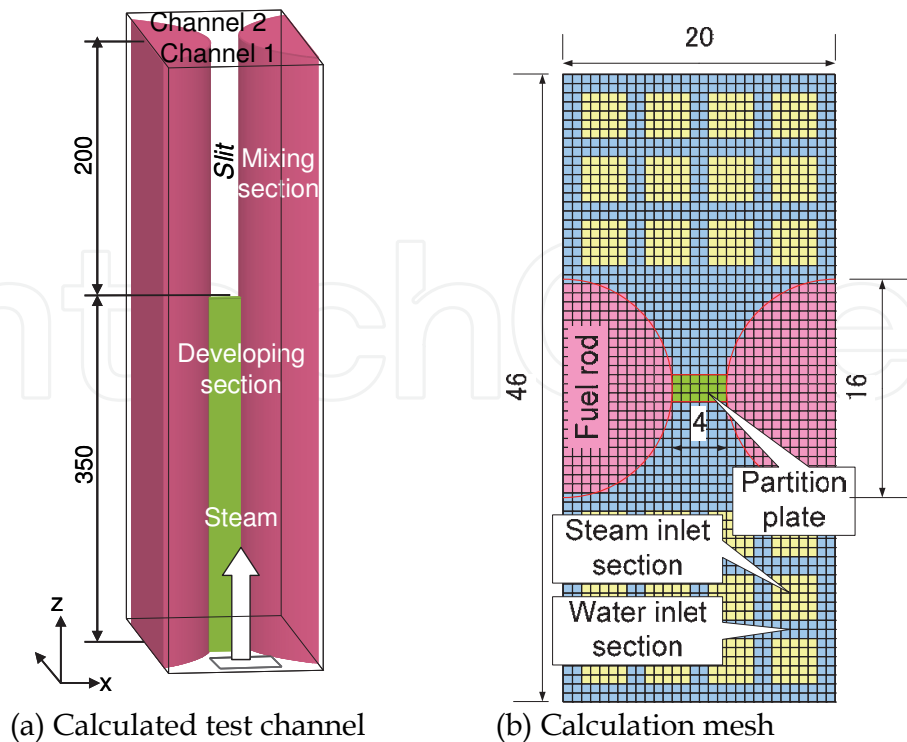


Fig. 21. Dimensions of calculated test channel and calculation meshes for BWR cases.

The calculated test channel is shown in Fig.21 (a) and Fig.22 (a). The flow area is divided into two channels by a flat plate (partition plate) as same as the air-water cases. The flow channel is divided into 2 parts, developing section and mixing section. Liquid phase velocity in the BWR cases and the FLWR cases is relatively higher than that in air-water cases. To remove the effects on flow development and fluid mixing, length of the developing section and the mixing section were extended and the outlet section was removed.

Case	Gap width (mm)	Inlet liquid mass flux (kg/m ² s)		Inlet quality (%)		
		Ch.1	Ch.2	Ch.1	Ch.2	
F1	1.3	600	150	0.05	0.21	
F2			600		0.05	0.002
F3						0.03
F4						0.08
F5	1.0	600	600	0.05		0.05
F6					0.03	
F7					0.08	
F8					0.12	

Table 7. Calculation conditions for fluid mixing phenomena in FLWRs fuel bundle.

Regular mesh division in the Cartesian system was adopted except for lower part of the developing section. In the lower part of developing section ($z=0\sim 350$ mm for BWR cases, $z=0\sim 200$ mm for FLWR cases), to save computational resources, a relatively coarse computational meshes were used ($\Delta z=2$ mm). The other region, Δz equals to 1mm. Two subchannels and the interconnection were formed by using obstacles. The calculation mesh

size was set to 2/3 mm for BWR cases and 0.21mm or 0.16mm for FLWR cases to satisfy the condition that the number of the calculation meshes of gap region must be more than 6. A non-slip wall, constant exit pressure and constant inlet velocity were selected as boundary conditions for each subchannel.

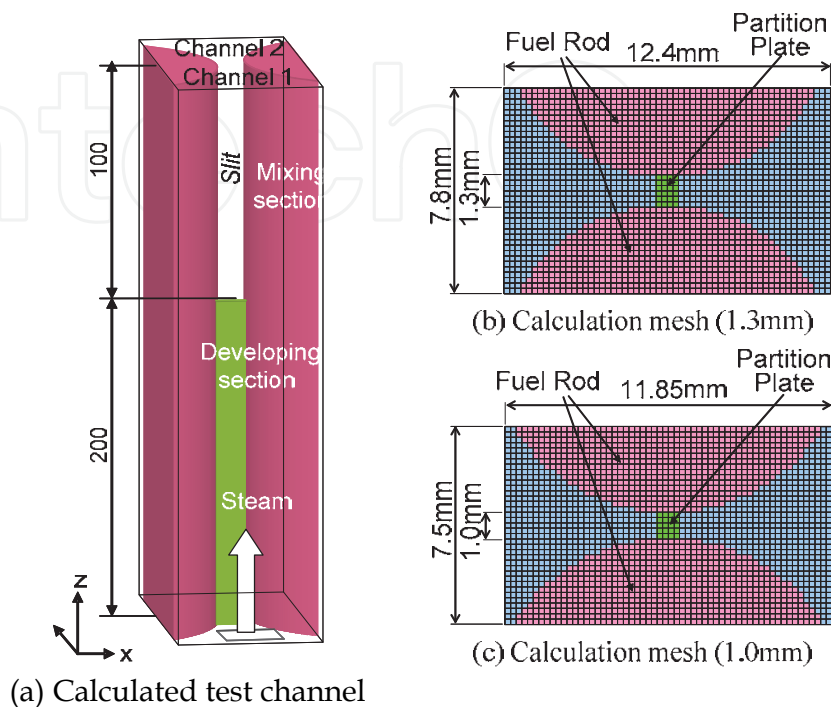


Fig. 22. Dimensions of calculated test channel and calculation meshes for FLWR cases.

To simulate the operating conditions of the BWR and the FLWR, outlet pressure and inlet temperature of steam and water is set to 7 MPa and saturation temperature at 7 MPa respectively. Steam and water were injected through the steam and water inlet section located at lower part of the modeled test channel. The steam and water inlet sections were optimized to get a developed flow at inlet of test section, and divided into twelve small sections for BWR cases.

4.1.2 Evaluation of existing correlations

Example of the calculated behaviors in the test channel and detail of slug behavior of are shown in Fig.23. As shown in Fig.23, the fluid mixing between Ch.1 and Ch.2 was observed at a gap between the subchannels. Though inlet quality of both subchannels were equivalent in this case (inlet quality ratio (X_2/X_1) was equal to 1.0), fluid mixing occurred between 2 subchannels.

The existing two-phase flow correlation for fluid mixing (fluctuating pressure model (Takemoto, 1997) was evaluated using detailed numerical simulation data. The fluctuating pressure model is expressed as follows:

$$|w_T| = \sqrt{\frac{2\rho_l |\Delta p_T|}{K(1-x)^2 \left[1 + Bx \left(\frac{\rho_l}{\rho_g} - 1 \right) \right]}} = f(x) \sqrt{|\Delta p_T|} \quad (21)$$

where,

w_T : evaluated moved mass flow rate by the fluctuating pressure model [kg/s]

K : time averaged pressure loss coefficient [-]

x : time averaged quality [-]

B : time averaged two-phase flow pressure loss coefficient [-]

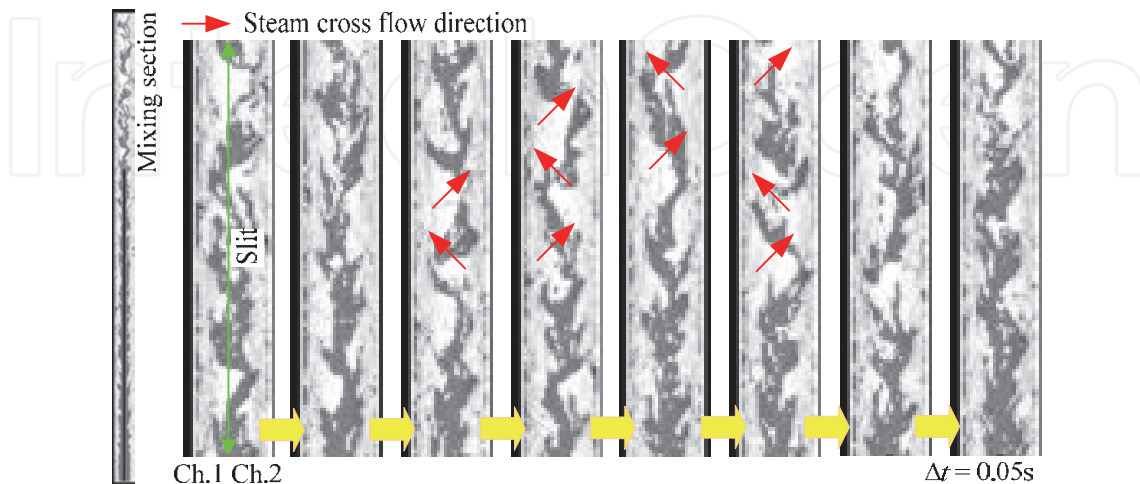


Fig. 23. Calculated slug behavior of case F5 in mixing section.

By the fluctuating pressure difference model, mixing coefficients for both phases are evaluated by following equations.

$$\Gamma_{m,T} = \frac{\overline{w_{m,T}}}{W_{m1} + W_{m2}} \quad (22)$$

where,

$$w_{l,T} = -(1-x) f(x) \frac{\Delta p_T}{\sqrt{|\Delta p_T|}}, w_{g,T} = -x f(x) \frac{\Delta p_T}{\sqrt{|\Delta p_T|}} \quad (23)$$

In above equations, instantaneous pressure difference values and time averaged values (pressure loss coefficient, quality and two-phase flow pressure loss coefficient) are evaluated by numerical results.

To estimate effects of fluctuating pressure on the mixing coefficients, the mixing coefficients using time averaged pressure difference were also evaluated for BWR cases:

$$\Gamma_{m,S} = \frac{w_{m,S}}{W_{m1} + W_{m2}} \quad (24)$$

where,

$$w_{l,S} = -(1-x) f(x) \frac{\Delta p_s}{\sqrt{|\Delta p_s|}}, w_{g,S} = -x f(x) \frac{\Delta p_s}{\sqrt{|\Delta p_s|}} \quad (25)$$

Evaluated mixing coefficients by fluctuating pressure model, $\Gamma_{m,T}$ are shown in Fig.24. Predicted mixing coefficients by TPFIT code and $\Gamma_{m,S}$ are also shown in figures. The

evaluated mixing coefficients, $\Gamma_{m,T}$ were in reasonable agreement with the predicted results. Evaluated mixing coefficients by use of time averaged pressure difference, $\Gamma_{m,S}$ overestimated the predicted results in almost all cases, and it is understood that the fluctuating component of pressure difference restrains the fluid mixing between subchannels.

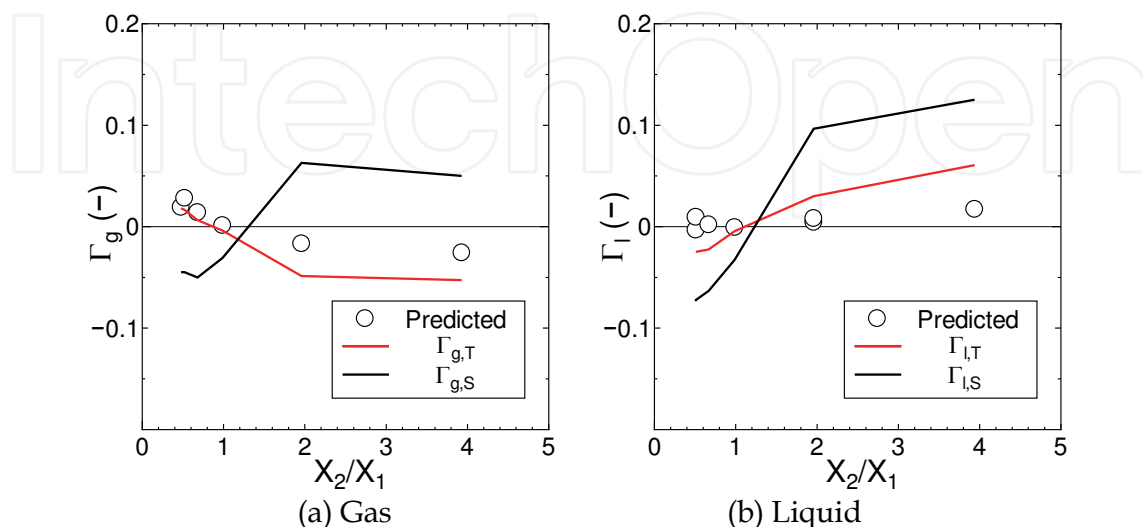


Fig. 24. Evaluation of the fluctuating pressure model for BWR cases (Case B1~B8).

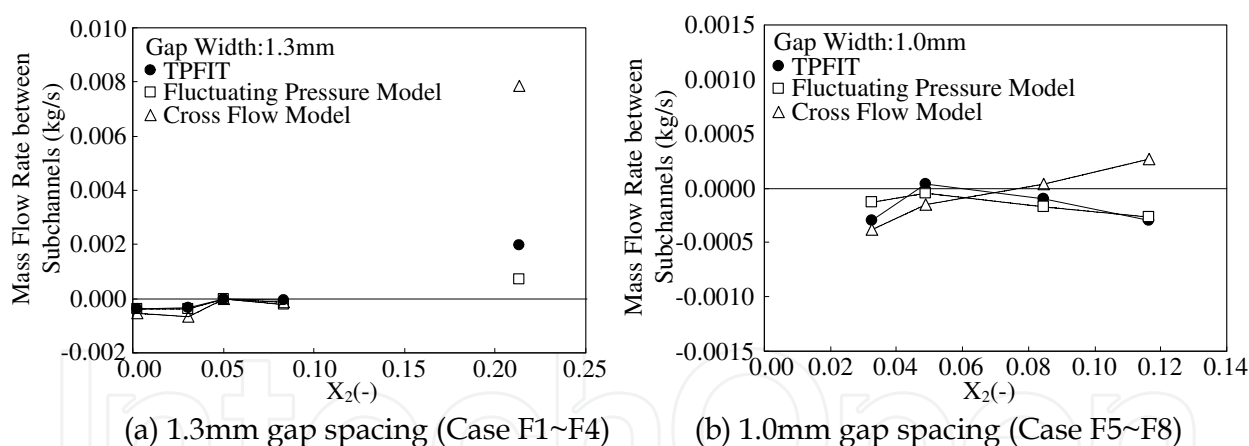


Fig. 25. Evaluation of the existing correlations for FLWR cases (Case F1~F8).

Evaluated mixing coefficients by fluctuating pressure model and conventional fluid mixing model (Kelly and Kazimi, 1980) for FLWR cases are shown in Fig.25. Predicted mixing coefficients by the TPFIT are also shown in figures. The evaluated mixing coefficients by fluctuating pressure model for relatively low inlet quality cases were in reasonable agreement with the predicted results for both 1.3 mm and 1.0 mm gap spacing. However, evaluated mixing coefficients by conventional fluid mixing model were different from predicted mixing coefficients by the TPFIT code both qualitatively and quantitatively. Evaluated mixing coefficients for relatively high inlet quality cases (inlet quality ratio (X_2/X_1) is large) by fluctuating pressure model and conventional fluid mixing model showed underestimation and overestimation respectively.

4.2 Development of correlation base on detailed numerical simulation results

In section 4.1, existing correlations for the two-phase flow fluid mixing phenomena were examined. However, enough results were not obtained. Then, we try to develop new correlation for fluid mixing phenomena in tight lattice rod bundle based on numerical results.

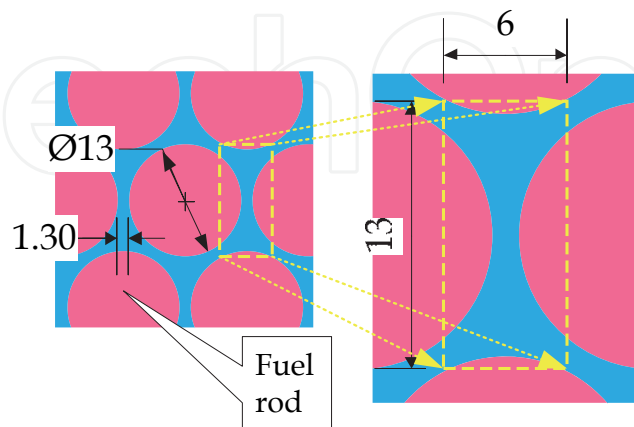


Fig. 26. Simulated region in rod bundle.

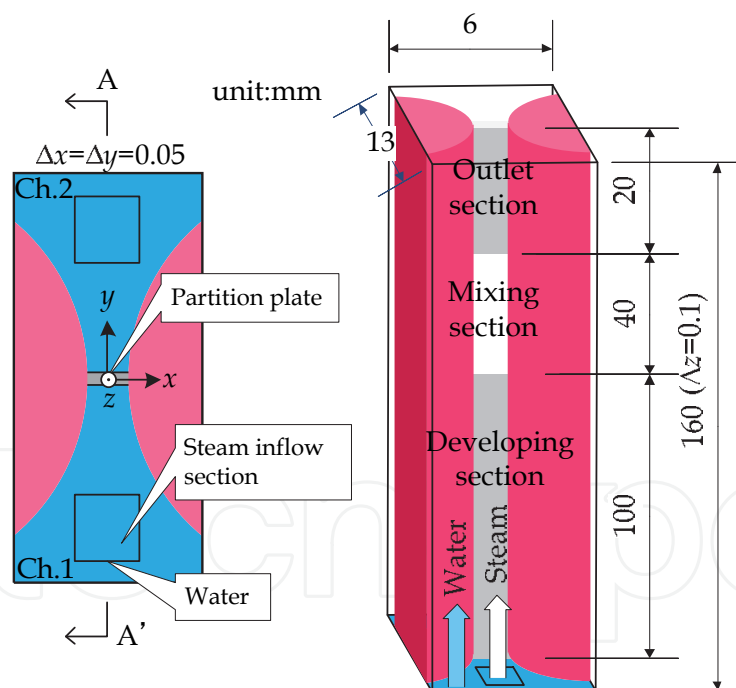


Fig. 27. Modeled two sub-channels.

The simulated region in a tight-lattice rod bundle is schematically shown in Fig.26. The diameter of fuel rods is 13.0mm. The smallest gap spacing between two adjacent fuel rods is 1.3mm. Numerical domain used in this simulation is shown in Fig.27. The length and width of the simulated region are 13.0mm and 6.0mm respectively. The two subchannels are separated by a partition plate with the thickness of 0.2mm, in the upper part of which there is a slit with the height of 40mm. Water and steam flow into the subchannels through the

bottom. Gas and liquid flows pass through three sections along the axial direction, i.e. developing, mixing and outlet sections. Grid numbers are $120 \times 260 \times 1600$ (49,920,000). Saturated water and steam at 7.2MPa are used as working fluids. Steam and liquid are injected at constant velocities with values tabulated. The total mass flux is set to $400 \text{ kg/m}^2\text{s}$.

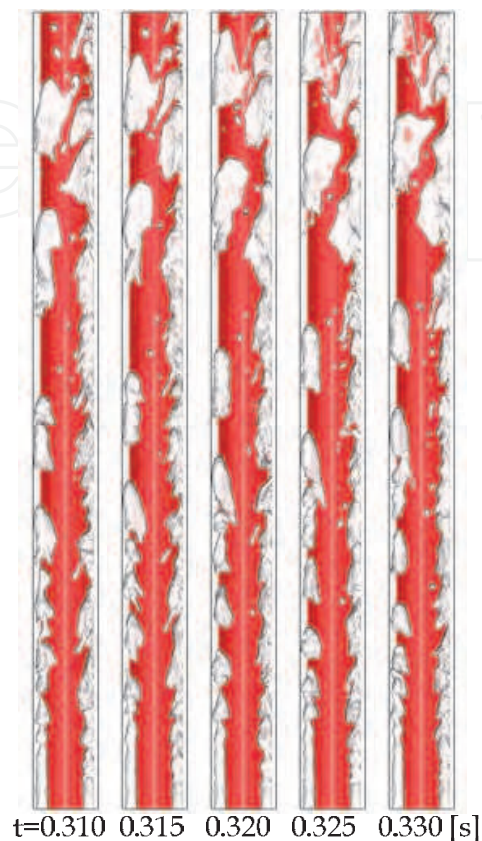


Fig. 28. Examples of simulation results.

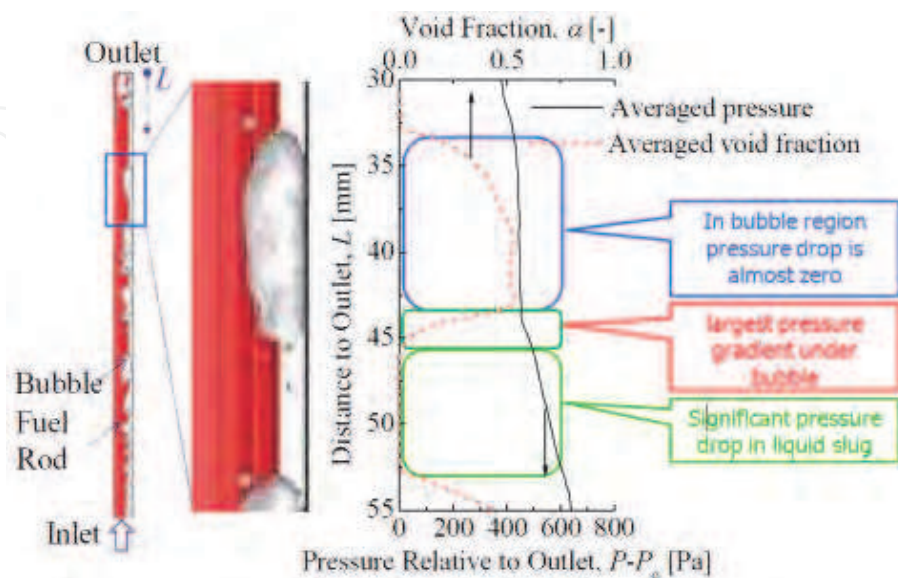


Fig. 29. Axial cross-sectional averaged pressure and void fraction distribution.

Figure 28 shows the time change of void fraction distribution observed from the section A-A', as indicated in Fig.27. The red color denotes the fuel rod. It can be seen that the gas phases cross the slit mutually. Figure 29 shows the axial cross-sectional pressure and void distributions around a slug bubble. It illustrates that most of pressure gradient takes place in liquid slug zone and the pressure almost keeps constant in large bubble zone. Below the bubble, there exists large pressure gradient. This is reasonable because flow after the bubble is highly disturbed and vortexes may occur there.

In simulation results, strong correlation for liquid phase means that liquid fluid mixing occurs due to local inter-subchannel differential pressure. Then we decided to develop an approximate model for prediction of differential pressure between subchannels. Pressure difference between subchannels is induced by difference of axial pressure distribution in each subchannel. Therefore, to evaluate mixing flow rate between subchannels by fluid mixing phenomena, axial pressure distribution in subchannels must be required. In following section, axial pressure distribution (axial pressure loss) model is developed.

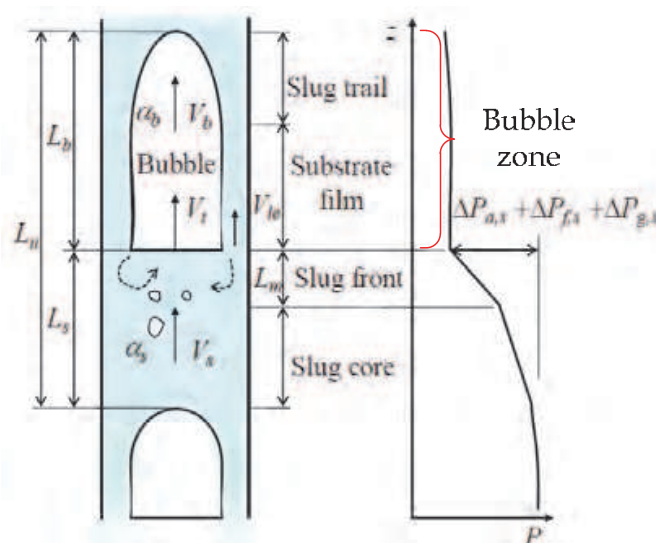


Fig. 30. Physical model for slug flow.

Based on the above-mentioned results of the numerical simulation, we considered pressure distributions in bubble zone, slug front and slug core (see Fig.30). In the bubble zone, the pressure almost keeps constant in this zone. Therefore, pressure drop across a bubble zone is assumed to be zero as follows:

$$\frac{dP_b}{dz} = 0 \quad (26)$$

In slug front and slug core, there are three contributions to the pressure drop across a slug. The first, $dP_{a,s}$, is the pressure drop that results from the acceleration of the slow moving liquid film to slug velocity in the slug front zone. The second, $dP_{f,s}$, is the pressure drop required to overcome wall shear. The third, $dP_{g,s}$, is the static head pressure drop. The total pressure gradient across a liquid slug is thus given by

$$\frac{dP_s}{dz} = \frac{dP_{a,s}}{dz} + \frac{dP_{f,s}}{dz} + \frac{dP_{g,s}}{dz} \quad (27)$$

In the slug front region, flow after the bubble is highly disturbed and vortices may occur there. Then additional pressure loss must be considered. A slug that has stabilized in length can be considered as a body receiving and losing mass at equal rates. The velocity of the liquid in the film just before pickup is lower than that in the slug and a force is therefore necessary to accelerate this liquid to slug velocity. This force manifests itself as a pressure drop. If the pressure along the liquid film in the bubble zone can be assumed to be essentially constant, this force can be evaluated by the sum of gravity and wall shear stress in the liquid film zone (Taitel and Barnea, 1990). Here the following equations are employed to evaluate the acceleration pressure drop for vertical flow:

$$\Delta P_a = \frac{W_{le}}{A} (V_s - V_{le}), \quad (28)$$

where W_{le} is the rate at which mass is picked up by the liquid slug, which can be obtained from the following equation:

$$W_{le} = \rho_l \cdot A \cdot (1 - \alpha_{le}) \cdot (V_l - V_{le}) \quad (29)$$

where α_{le} , V_{le} are the void fraction and mean velocity of liquid film at front of liquid slug. V_l is the propagation velocity of the slug unit or average translational velocity of the nose of the slug, given by Taitel and Barnea (1990)

$$V_l = 1.2V_s + 0.35\sqrt{gD_b} \quad (30)$$

Here, D_b is the bubble diameter, which may be approximately estimated from the average void fraction of the bubble zone, α_b .

$$D_b = \sqrt{A \cdot \alpha_b} \quad (31)$$

where

$$\alpha_b = \frac{1}{L_b} \int_0^{L_b} \alpha_l dx \quad (32)$$

Here α_l is the local void fraction in the bubble zone. In Eq.(28), the mean velocity of fluid in the slug, V_s , is given as

$$V_s = \frac{1}{A} \left(\frac{W_l}{\rho_l} + \frac{W_g}{\rho_g} \right) \quad (33)$$

The pressure drop due to acceleration takes place in the slug front which penetrates a distance into the body of the slug. The depth of penetration of the liquid film into the slug appears to depend on the relative velocity between slug and film, and may be obtained from the following equation (Dukler and Hubbard, 1975).

$$L_{sf} = 0.3 \cdot \frac{\rho_l (V_s - V_{ls})^2}{2} \quad (34)$$

And the acceleration gradient in the slug front is given by,

$$\frac{dP_{a,s}}{dz} = \frac{\Delta P_a}{L_{sf}} \quad (35)$$

In the slug front and slug core region, frictional and gravity pressure drop are acting in subchannels. Frictional pressure drop takes place when liquid slug moves along the channel wall. For the calculation of this term, the similarity analysis for two-phase frictional pressure drop (Dukler et al., 1975) is applied. Within the liquid slug the bubble size is usually small and thus the flow can be deemed as the homogeneous one with negligible two-phase slip. Under this condition, the frictional pressure drop can be calculated as follows:

$$\frac{dP_{f,s}}{dz} = \frac{2f_s}{D_h} [\rho_l(1-\alpha_s) + \rho_g\alpha_s] \cdot V_s^2 \quad (36)$$

For “non-slip” conditions f_s could be correlated as a unique function of Re_s

$$f_s = 0.079 \cdot Re_s^{-0.025} \quad (37)$$

Here the Reynolds number Re_s is defined in the following manner:

$$Re_s = D_h V_s \frac{\rho_l(1-\alpha_s) + \rho_g\alpha_s}{\mu_l(1-\alpha_s) + \mu_g\alpha_s} \quad (38)$$

The static head term for the slug front and slug core can be obtained from the following simple equation:

$$\frac{dP_{g,s}}{dz} = [\rho_l(1-\alpha_s) + \rho_g\alpha_s] \cdot g \quad (39)$$

The axial relative pressure in question could be obtained through the integration of differential pressure as follows

$$P = \int_0^z \frac{dP}{dz} dz \quad (40)$$

$$\frac{dP}{dz} \begin{cases} \frac{dP_s}{dz} & \text{in slug zone} \\ \frac{dP_b}{dz} & \text{in bubble zone} \end{cases}$$

The above equations are incomplete and some parameters are still unknown, such as local void fraction in the bubble zone α_l , the mean velocity of liquid film at front of liquid slug, the bubble length L_b as well as that of slug unit L_{sl} , and instantaneous bubble distribution. These parameters may be predicted by assuming the idealized bubble shape and setting the initial bubble distribution along the channel. We leave them for future study. In this study we aim at exploring the mechanism of differential pressure fluctuation inducing cross flow as a first step, therefore numerical simulation results are used to evaluate these unknown parameters for simplicity. In addition, a criterion to reduce the detailed three-dimensional simulation results is introduced to determine locations and lengths of bubble zones (or slug zones). The regions, where the cross-sectional averaged void fraction is larger than 0.3, are deemed as bubble zones. Other regions are regarded as slug zones.

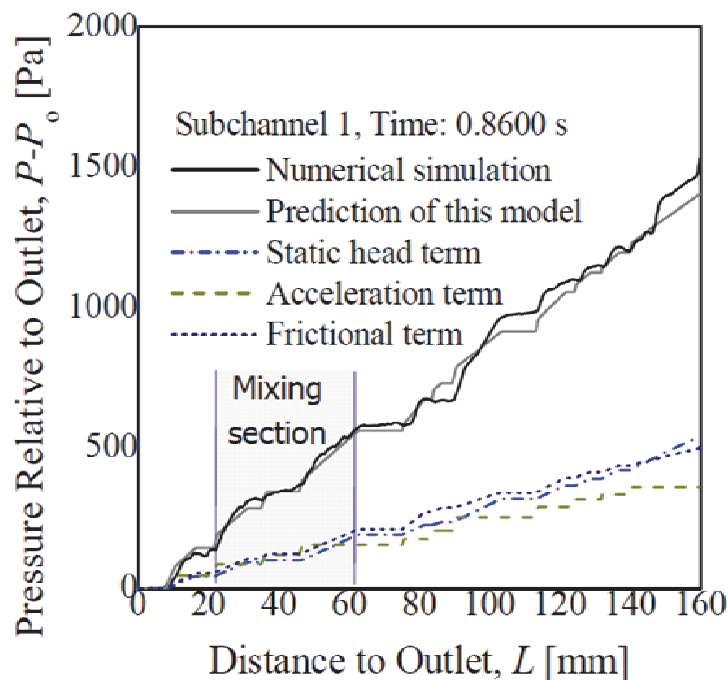


Fig. 31. Instantaneous axial pressure distribution.

Here, the model is evaluated with the axial pressure profile obtained from the numerical simulation for a subchannel with cross flow. Figure 31 shows the evaluation results at an instant with time of 0.8600 s. From the figure, it can be seen that the prediction of the model is generally in agreement with the simulation results, especially for mixing section (abscissa from 20 mm to 60 mm). This means the model may be applicable to subchannels. And furthermore, we can see that the three contributions to pressure drop have almost similar weights in the total pressure drop.

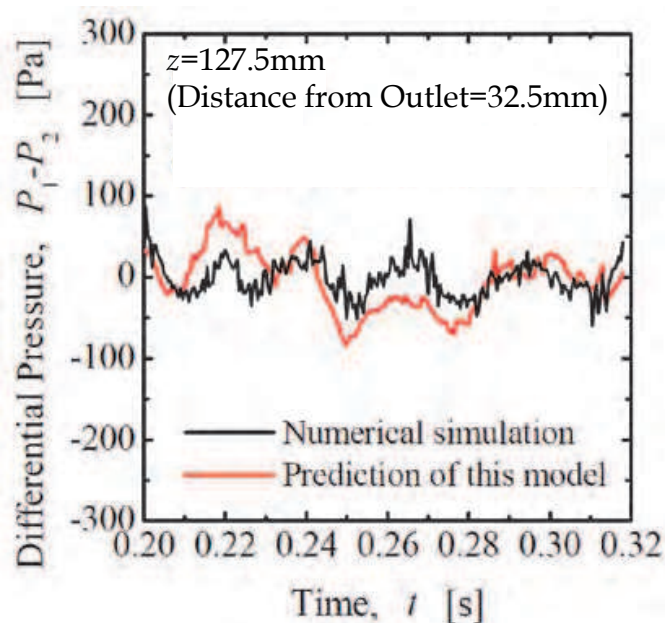


Fig. 32. Fluctuation of differential pressure between two subchannels.

In this study, the way to evaluate the cross-section averaged pressure distribution in a single subchannel has been developed. If we assume that cross flow has minor effect on the pressure distribution in each subchannel, we can evaluate the pressure differences between subchannels by axial pressure distribution for each subchannel. In this way, the prediction of differential pressure by the model is compared to that obtained from the numerical simulation as shown in Fig. 32. It can be seen that the prediction of this model may reproduce the results of numerical simulation generally. For the time of 0.22 or 0.27, cross flow may have not negligible effect on inter-subchannel differential pressures and thus predictions deviate from the simulation results.

5. Conclusion

To perform thermal hydraulic design of the boiling water reactor (BWR) without actual size tests, we have been developed a new design method for BWRs. In this design method, the two-phase flow correlations for fluid mixing phenomena must be modified or created based on results of large scale numerical simulations. Then, we developed an innovative two-phase flow simulation code TPFIT and an advanced interface tracking method. In the advanced interface tracking method, gas and liquid mass conservation equations are solved, to treat compressibility of gas and to keep high volume conservation of gas and liquid.

In the second step, to verify and validate the TPFIT with the advanced interface tracking method, the TPFIT was applied to some experimental analyses including three the 2-channel fluid mixing tests, and comparisons between measured and predicted result were carried out. By these results, it was concluded that the TPFIT can be applied to the two-phase flow fluid mixing phenomena.

In the next step, the TPFIT was applied to the numerical simulation of fluid mixing between subchannels on a current BWR and FLWR that is one of innovative water reactor concept developed in JAEA. The existing two-phase flow correlation for fluid mixing was evaluated using detailed numerical simulation data. When inlet quality ratio of subchannels is relatively large, evaluated mixing coefficients by existing two-phase flow correlations for fluid mixing were different from those of the detailed numerical simulation data. And new correlation based on large scale numerical simulation results are expected.

In the fourth step, we tried to develop new two-phase flow correlations related to the fluid mixing phenomena. Differential pressure fluctuation between subchannels dominates the fluid mixing phenomena. We considered that the differential pressure fluctuation is induced by difference of axial pressure distribution in each subchannel. Then we developed new correlation for axial pressure distribution. In this correlation, a hydrostatic gradient, acceleration and frictional gradients are taken into account in the liquid slug, and no pressure gradient exists in the slug bubble. New correlation was validated by numerical results of the TPFIT, and it was concluded that predicted results of this correlation almost agree with the simulation results. Furthermore, differential pressure fluctuation based on predicted axial pressure distribution in subchannels can predict differential pressure by the TPFIT. We thought that the method to create new two-phase flow correlations by results of large scale numerical simulations is effective. However, there is issue such as required computational resources or validation of prediction accuracy of created correlations.

6. Acknowledgment

This research was conducted using a supercomputer of the Japan Atomic Energy Agency.

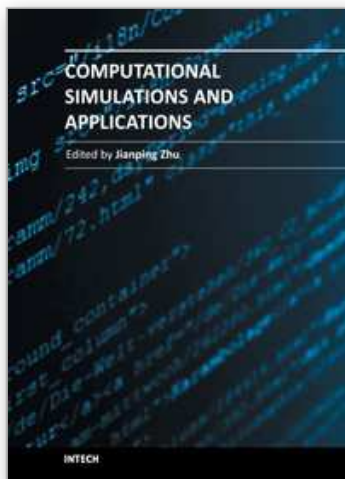
7. References

- Lahey, Jr, R. T. & Moody, F. J., (1993), *The Thermal-Hydraulics of a Boiling Water Nuclear Reactor*, American Nuclear Society, La Grange Park, Illinois USA.
- Kawahara, A., Sadatomi, M. & Tomino, T., (2000), Prediction of Gas and Liquid Turbulent Mixing Rates between Rod Bundle Subchannels in a Two-Phase Slug-Churn Flow, *Trans. JSME, Ser. B*, 66, pp. 1191-1197
- Sumida, I., Yamakita, T., Sakai, S., Iwai, K., & Kondo, T., (1995), Investigation of Two-Phase Flow Mixing between Two Subchannels (1st Report, Fluctuating Pressure Model and its Experimental Verification), *Trans. JSME, Ser. B*, 61, pp. 2662-2668 (in Japanese).
- Takemoto, S., Kondo, T., Inatomi, T., Sakai, S., Wakai, K., & Sumida, I., (1997), Investigation of Two-Phase Flow Mixing between Two Subchannels (2nd Report, Verification of Fluctuating Pressure Model without Steady Pressure), *Trans. JSME, Ser. B*, 61, pp. 3107-3113 (in Japanese).
- Yabe, T., & Aoki, T., (1991), A Universal Solver for Hyperbolic Equations by Cubic-Polynomial Interpolation I. One-Dimensional Solver, *Comput.Phys.Commun.*, 66, pp. 219-232.
- Brackbill, J. U., Kothe, D. B., & Zemach, C., (1992), A Continuum Method for Modeling Surface Tension, *J. Comput. Phys.*, 100, pp. 335-354.
- Gueyffier, D., Nadim, J. Li, A., Scardovelli, R., & Zaleski, S., (1999), Volume-of-Fluid Interface Tracking with Smoothed Surface Stress Methods for Three-Dimensional Flows, *J. Comput. Phys.*, 152, pp. 423-456.
- Rayleigh, L., (1879), On the Capillary Phenomena of Jets, *Proc. R. Soc. London*, 29, p. 71-97.
- Moran, K., Inumaru, J., & Kawaji, M., (2002), Instantaneous hydrodynamics of a laminar wavy liquid film, *Int. J of Multiphase Flow*, 28 pp.731-755.
- Nusselt, W., (1916), Die oberflächenkondensation des wasserdampfes, *VDI-Zs* 60, 541.
- Yoshida, H., Nagayoshi, T., Takase, K., & Akimoto, H., (2007), Development of Design Technology on Thermal-Hydraulic Performance in Tight-Lattice Rod Bundles: IV - Numerical Evaluation of Fluid Mixing Phenomena using Advanced Interface-Tracking Method -, *Proc. of ICONE15 (CD-ROM)*, Nagoya, Japan, September 22-26, 10532.
- Uchikawa, S., Okubo, T., Kugo, T., Akie, H., Takeda, R., Nakano, Y., Ohnuki, A., & Iwamura, T., (2007), Conceptual Design of Innovative Water Reactor for Flexible Fuel Cycle (FLWR) and its Recycle Characteristics, *J. Nucl. Sci. Tech.*, 44, 3, pp.277-284.
- Taitel, Y., & Barnea, D., (1990), Two-Phase Slug Flow, *Advances in Heat Transfer*, 20, pp. 83-132

- Dukler, A. E., & Hubbard, M. G., (1975), A model for gas-liquid slug flow in horizontal and near horizontal tubes, *Ind. Eng. Chem., Fundam.*, 14, pp. 337-347.
- Kelly, J.E., & Kazimi, M.S., (1980), Development of the two-fluid multidimensional code THERMIT for LWR analysis, *AIChE Symposium Series*, pp. 149-162.

IntechOpen

IntechOpen



Computational Simulations and Applications

Edited by Dr. Jianping Zhu

ISBN 978-953-307-430-6

Hard cover, 560 pages

Publisher InTech

Published online 26, October, 2011

Published in print edition October, 2011

The purpose of this book is to introduce researchers and graduate students to a broad range of applications of computational simulations, with a particular emphasis on those involving computational fluid dynamics (CFD) simulations. The book is divided into three parts: Part I covers some basic research topics and development in numerical algorithms for CFD simulations, including Reynolds stress transport modeling, central difference schemes for convection-diffusion equations, and flow simulations involving simple geometries such as a flat plate or a vertical channel. Part II covers a variety of important applications in which CFD simulations play a crucial role, including combustion process and automobile engine design, fluid heat exchange, airborne contaminant dispersion over buildings and atmospheric flow around a re-entry capsule, gas-solid two phase flow in long pipes, free surface flow around a ship hull, and hydrodynamic analysis of electrochemical cells. Part III covers applications of non-CFD based computational simulations, including atmospheric optical communications, climate system simulations, porous media flow, combustion, solidification, and sound field simulations for optimal acoustic effects.

How to reference

In order to correctly reference this scholarly work, feel free to copy and paste the following:

Hiroyuki Yoshida and Kazuyuki Takase (2011). Development of Two-Phase Flow Correlation for Fluid Mixing Phenomena in Boiling Water Reactor, Computational Simulations and Applications, Dr. Jianping Zhu (Ed.), ISBN: 978-953-307-430-6, InTech, Available from: <http://www.intechopen.com/books/computational-simulations-and-applications/development-of-two-phase-flow-correlation-for-fluid-mixing-phenomena-in-boiling-water-reactor>

INTECH
open science | open minds

InTech Europe

University Campus STeP Ri
Slavka Krautzeka 83/A
51000 Rijeka, Croatia
Phone: +385 (51) 770 447
Fax: +385 (51) 686 166
www.intechopen.com

InTech China

Unit 405, Office Block, Hotel Equatorial Shanghai
No.65, Yan An Road (West), Shanghai, 200040, China
中国上海市延安西路65号上海国际贵都大饭店办公楼405单元
Phone: +86-21-62489820
Fax: +86-21-62489821

© 2011 The Author(s). Licensee IntechOpen. This is an open access article distributed under the terms of the [Creative Commons Attribution 3.0 License](#), which permits unrestricted use, distribution, and reproduction in any medium, provided the original work is properly cited.

IntechOpen

IntechOpen